Experimental test of the viscous anisotropy hypothesis for partially molten rocks

Chao Qi (綦超)[a,1,2], David L. Kohlstedt[a], Richard F. Katz[b], and Yasuko Takei (武井康子)[c]

[a]Department of Earth Sciences, University of Minnesota, Minneapolis, MN 55455; [b]Department of Earth Sciences, University of Oxford, Oxford OX1 3AN, United Kingdom; and [c]Earthquake Research Institute, University of Tokyo, Tokyo 113-0032, Japan

Edited by David Walker, Columbia University, Palisades, NY, and approved September 2, 2015 (received for review July 14, 2015)

Chemical differentiation of rocky planets occurs by melt segregation away from the region of melting. The mechanics of this process, however, are complex and incompletely understood. In partially molten rocks undergoing shear deformation, melt pockets between grains align coherently in the stress field; it has been hypothesized that this anisotropy in microstructure creates an anisotropy in the viscosity of the aggregate. With the inclusion of anisotropic viscosity, continuum, two-phase-flow models reproduce the emergence and angle of melt-enriched bands that form in laboratory experiments. In the same theoretical context, these models also predict sample-scale melt migration due to a gradient in shear stress. Under torsional deformation, melt is expected to segregate radially inward. Here we present torsional deformation experiments on partially molten rocks that test this prediction. Microstructural analyses of the distribution of melt and solid reveal a radial gradient in melt fraction, with more melt toward the center of the cylinder. The extent of this radial melt segregation grows with progressive strain, consistent with theory. The agreement between theoretical prediction and experimental observation provides a validation of this theory.

viscous anisotropy | melt segregation | partial melts | basalt | olivine

Shear deformation of partially molten rocks gives rise to melt segregation into sheets (bands in cross-section) that emerge at a low angle to the shear plane. This mode of segregation was predicted with two-phase flow theory (1) and subsequently discovered in experiments (2, 3). It has been proposed that melt-enriched bands, if present in the mantle of Earth, would permit rapid extraction of melt (4), produce significant anisotropy in seismic wave propagation (5), and provide a mechanism for the seismic discontinuity that is, in some places, associated with the lithosphere–asthenosphere boundary (6). The emergence (7) and low angle (8) of melt-enriched bands under simple-shear deformation can be reproduced using two-phase flow theory with a non-Newtonian, isotropic viscosity. This theory describes the flow of a low-viscosity liquid (melt) through a permeable and viscously deformable solid matrix (grains) (9). However, an unrealistically strong stress dependence of viscosity was required to match the low angle of bands observed in experiments (8). This disagreement between models and experiments found a possible resolution by the incorporation of anisotropic viscosity arising from coherent alignment of melt pockets between grains [i.e., melt-preferred orientation (MPO)] in response to a deviatoric stress (10–13).

Crucially, with the inclusion of viscous anisotropy, two-phase flow theory also predicts a simultaneous but distinct mode of melt segregation driven by large-scale gradients in shear stress. This mode is termed base-state melt segregation (13–15). Base-state melt segregation is not predicted if viscosity is isotropic; thus, its occurrence in experiments represents a test of the hypothesis that MPO leads to anisotropy in viscosity. Below we explain base-state melt segregation in more detail; we then present new experimental results that demonstrate its occurrence.

Fig. 1*A* illustrates how anisotropy in grain/melt microstructure (i.e., MPO) produces viscous anisotropy through the mechanics of diffusion creep (10). For a representative grain in an aggregate subjected to a deviatoric stress, the contact area with neighboring grains decreases for grain boundaries that are normal to the direction of the minimum principal stress σ_3 (the minimum eigenvalue of the deviatoric stress tensor, compression positive). A decrease in contact area shortens the diffusion pathway for material transport along this boundary relative to grain boundaries with different orientations. Because melt provides a fast pathway for diffusion, this change in the contiguity between neighboring grains reduces the timescale of the diffusive response to the σ_3 component of stress. Conversely, an increase in grain–grain contact area normal to the direction of the maximum principal stress σ_1 lengthens the diffusion pathway on this surface and thus the timescale for diffusive response to stress in this direction.

To translate these concepts from the microscopic to the continuum scale, consider a representative element of volume (REV) that is large enough to contain many microscopic units (grains and melt pockets) and small enough to define a point property at the scale of macroscopic features of interest (Fig. 1*B*). Under deviatoric stress, melt pockets in the REV coherently align normal to the σ_3 direction and the timescale for the diffusive response to stress is reduced in this direction. If the dominant deformation mechanism of the aggregate is diffusion creep, this rapid response imparts a reduction of the continuum viscosity in the σ_3 direction (10, 16). Likewise, the change in grain contiguity associated with σ_1 increases the viscosity in that direction.

Viscous anisotropy can be quantified with a highly symmetric, fourth-rank tensor (*SI Appendix 1*). The orientation of this tensor is described by three angles that rotate it with respect to the system coordinates. This rotation is used to align anisotropy with the principle directions of deviatoric stress. As a simplifying

Significance

Partially molten regions of Earth link mantle convection with surface volcanism. We present laboratory experiments and theory that are at the heart of understanding the connection between these interior and surface processes. The theory proposes that the presence of melt fundamentally changes the style of deformation, making it anisotropic with leading-order, testable consequences. The laboratory results are in agreement with theoretical predictions. These results are novel at a foundational level and profoundly surprising. Together they make the case that the creep rheology of partially molten rocks is more than the sum of its parts. Moreover, this article sets forth a framework that will guide a broad swath of future research in rock mechanics and mantle flow.

Author contributions: C.Q. and D.L.K. designed research; C.Q., D.L.K., R.F.K., and Y.T. performed research; C.Q. analyzed data; and C.Q., D.L.K., R.F.K., and Y.T. wrote the paper.

The authors declare no conflict of interest.

This article is a PNAS Direct Submission.

[1]Present address: Department of Earth and Environmental Science, University of Pennsylvania, Philadelphia, PA 19104-6316.

[2]To whom correspondence should be addressed. Email: chaoqi@sas.upenn.edu.

This article contains supporting information online at www.pnas.org/lookup/suppl/doi:10.1073/pnas.1513790112/-/DCSupplemental.

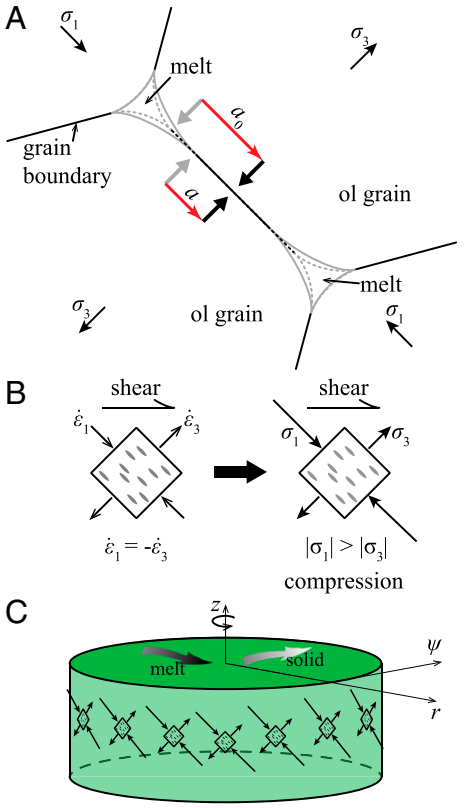

Fig. 1. Schematic diagrams of the interactions between stress and anisotropic viscosity. (*A*) Stress-induced melt redistribution and its influence on diffusion pathways in 2D. The grain boundaries in contact with a neighboring grain are in black, and the grain boundaries in contact with melt are in gray. Melt pockets under isotropic conditions are outlined with dashed lines, and the redistributed melt pockets under shear deformation are outlined with solid lines. Red arrows show the lengths of diffusion pathways from the grain-melt boundary (gray arrows) to the center of a grain boundary (black arrows). The diffusion pathway shortens from a_0 to a with applied deviatoric stress σ_3. (*B*) The coupling between torsional deformation with zero volumetric strain rate and stress with nonzero volumetric component associated with viscous anisotropy. The square is a REV with melt pockets (gray) aligned 45° to the shear plane, antithetic to the shear direction [modified from a previous study (13)]. (*C*) A sample-scale view of the development of the hoop stress from compressive stresses due to cylindrical geometry. In the cylindrical coordinates, z is the longitudinal axis parallel to the torsional axis, r is the polar axis along the radius, and ψ is the azimuthal axis.

approximation, we assume that, at each point in the domain, the imposed shear direction lies in the plane containing σ_1 and σ_3; this plane is perpendicular to the imposed shear plane (figures 3 and 5 of ref. 13). This leaves only one angle to be determined, the angle Θ between the shear plane and the σ_3 direction. The magnitude of anisotropy is parameterized with two scalars: α specifies the viscosity reduction in the σ_3 direction; β specifies the viscosity increase in the σ_1 direction. When either α or β or both α and β are nonzero at a point in the continuum, the viscosity at that point is anisotropic. The associated tensor then has nonzero off-diagonal terms that couple shear stress to normal strain rate (and vice versa). It is these terms that give rise to base-state segregation (13, 14).

To clarify the physical mechanism of base-state segregation, consider a cylindrical sample in a sealed chamber, deformed in torsion at a constant twist rate (Fig. 1*C*). Before any deviatoric stress is applied, the grain/melt microstructure is isotropic and the rate of (de)compaction is zero everywhere within the sample. With initiation of twisting, as a consequence of the deviatoric stress, a MPO develops and the viscosity becomes anisotropic. The imposed strain rate, aligned melt pockets, and consequent pattern of stress are shown schematically in Fig. 1 *B* and *C*. The disparity between $|\sigma_1|$ and $|\sigma_3|$ gives rise to a net compression that, because σ_1 and σ_3 are everywhere tangent to the cylinder, is a compressive hoop stress. This compressive hoop stress pushes the solid grains radially outward and causes a pressure gradient that drives melt radially inward (13) (details provided in *SI Appendix 2*). This differential motion is the base-state melt segregation under torsional deformation.

To test this prediction and hence the hypothesis that viscosity is anisotropic, we imposed a constant twist rate on cylindrical samples of partially molten rock that initially had uniform melt fraction (Table 1). In tangential sections of quenched samples that were deformed in torsion (Fig. 2), we observe aligned melt pockets and low-angle, melt-enriched bands. Melt-enriched bands are also evident in transverse sections (Fig. 3). More importantly, analyses of optical micrographs of transverse sections reveal a gradient in melt fraction in the radial direction, with melt concentrated toward the axis of the cylinder. This gradient in melt fraction corresponds to the base-state melt segregation predicted if viscosity is anisotropic. Our observations of MPO, melt-enriched bands, and radial melt segregation are detailed in subsequent paragraphs.

Results and Discussion

MPO. The rose diagram in Fig. 2*B* demonstrates that at a local shear strain of $\gamma = 4.6$, melt pockets are aligned at ~29° to the shear plane, antithetic to shear direction. In contrast, the expected σ_3 direction, based on cylindrical simple shear flow with isotropic viscosity, is 45° to the shear plane. The observed low angle of melt alignment means that, at this shear strain, either melt pockets are not normal to the σ_3 direction (17) or σ_3 has rotated counterclockwise. The reason for this alignment is unknown; it might be due to the emergence of chains of melt pockets (18) (Fig. 2*C*) or to the anisotropic viscosity itself. In the theory of two-phase flow with viscous anisotropy, elaborated in *SI Appendix 1*, it is generally assumed that melt pockets align perpendicular to σ_3, as suggested by deformation experiments on an analog material at small strains ($\gamma < 0.2$) (19). The observed MPO, therefore, may represent a subtle but important discrepancy between observation and theory that we return to below. Despite this possible discrepancy, the observed, strong MPO demonstrates the microstructural anisotropy that hypothetically causes viscous anisotropy.

Melt Distribution. Two-phase flow theory with anisotropic viscosity (13) also predicts the emergence of sheets of high-melt fraction that appear as bands in 2D sections (3). In Fig. 3, these features appear as radial lines of high-melt fraction where sheets cross the transverse section. For the sample deformed to an outer-radius shear strain of $\gamma(R) = 5.0$ (Fig. 3 *A* and *C*), the melt-enriched bands are distributed uniformly around the cylinder, whereas at a larger strain of $\gamma(R) = 14.3$ (Fig. 3 *B* and *D*), the

Table 1. Experiments summary

Sample	$\gamma(R)$*	$\dot{\varepsilon}_{eq}$, s^{-1}†	σ_{eq}, MPa†	ϕ_{max}/ϕ_{min}‡
PI0767	11.1	2.29×10^{-4}	187	1.6
PI0811	5.6	1.84×10^{-4}	237	1.2
PI0812	5.8	1.84×10^{-4}	163	1.4
PI0817	5.0	2.35×10^{-4}	197	1.3
PI0839	7.3	1.84×10^{-4}	237	1.7
PI0891	14.3	2.04×10^{-4}	179	2.0

*$\gamma(R)$ is the outer-radius shear strain, where R is the radius of a sample with $R \approx 6$ mm.
†The equivalent strain rate and stress, $\dot{\varepsilon}_{eq}$ and σ_{eq}, respectively, are calculated from shear strain rate and stress, using the Cauchy stress tensor.
‡ϕ_{max}/ϕ_{min} is the ratio of maximum to minimum melt fraction in the profile of azimuthally averaged melt fraction.

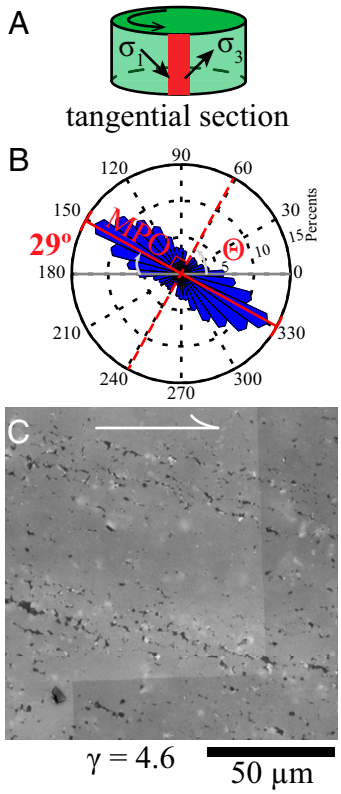

Fig. 2. MPO in a sample deformed to a shear strain of 4.6. (*A*) A sketch illustrating a deformed cylindrical sample with its tangential section marked in red. Arrows in this sketch illustrate the expected directions of deviatoric stresses σ_1 and σ_3 in tangential section. (*B*) A rose diagram generated from optical micrographs of the tangential section at a local shear strain of $\gamma = 4.6$ (PI0817). The rose diagram was constructed from more than 1,000 melt pockets with areas larger than 2 μm^2. The length of each petal represents the ratio of melt pockets with this certain orientation, scaled by percentage. Θ is anisotropy angle, which is the angle between red, dashed lines and 0°. (*C*) Optical micrograph from the tangential section of the sample. Olivine grains are light gray, melt is dark gray, and internal reflections or residual polishing material are white. The sense of shear is marked by the arrow on top.

azimuthal distribution of melt-enriched bands is inhomogeneous, dominated by several extraordinarily large bands. Because the total strain decreases toward the center of the cylinder, the region close to axial center exhibits less banding. More significantly, however, Fig. 3 *C* and *D* demonstrates a general increase in melt fraction toward the center of the cylinder, consistent with the predicted base-state migration of melt radially inward.

Radial profiles of the azimuthally averaged, normalized melt fraction are presented in Fig. 4*A* for seven experiments, each with a different final strain. The melt fraction in an experiment with no deformation (gray line) varies by less than 10% along a radius. In all deformed samples, the melt fraction increases toward the center of the cylinder—evidence for base-state segregation. For the three samples deformed to an outer-radius shear strain of $\gamma(R) = 5.5 \pm 0.5$, each radial profile of melt concentration reaches its peak at a radius of $r^{\text{peak}} \approx 1$ mm, corresponding to a shear strain of $\gamma(r^{\text{peak}}) \approx 1$. Melt fraction decreases from that point toward the axis of the cylinder; this behavior is expected because the low-stress/low-strain region at small radius has little or no MPO and hence has essentially isotropic viscosity ($\alpha = \beta = 0$). For samples deformed to higher outer-radius shear strains [$\gamma(R) = 7.3$, 11.1, and 14.3], peaks in melt fraction occur at a radius of $r^{\text{peak}} < 0.2$ mm. The sample with the highest outer-radius shear strain [$\gamma(R) = 14.3$] exhibits the largest ratio of maximum to minimum melt fraction $\phi_{\max}/\phi_{\min}$ (Table 1), a measure of the strength of base-state melt segregation. Except for the samples sheared to outer-radius shear strains of $\gamma(R) = 5.0$ and 7.3, the maximum in melt fraction increases with increasing shear strain. In summary, the results presented in Fig. 4*A* demonstrate that, with increasing strain, the pressure gradient induced by anisotropic viscosity drives melt inward, increasing the maximum value of the azimuthally averaged melt fraction and decreasing the radius at which this maximum occurs.

Comparisons with Model. Fig. 4*B* compares the azimuthally averaged profiles of normalized melt fraction from three samples deformed to $\gamma(R) = 5.5 \pm 0.5$ with those derived from numerical simulations. The data points in Fig. 4*B*, which are the mean values of the azimuthal averages at each radius, reach a maximum normalized melt fraction of ~1.15 at $r^{\text{peak}} \approx 1$ mm and a minimum of ~0.95 at $r \approx 4$ mm. For comparison, radial profiles of melt fraction from numerical simulations of samples deformed to $\gamma(R) = 5.5$ at an initial compaction length of $\delta_c = 0.1\ R$ and a bulk-to-shear viscosity ratio of $r_\xi = 10$. In the simulations, two conditions are used for the angle of viscous anisotropy: (*i*) Θ = 45°, suggested by previous experiments (19), and (*ii*) Θ = 60°, suggested by Fig. 2. For both conditions, if an initial perturbation in melt fraction is incorporated into the simulation, melt-enriched bands develop. However, for Θ = 60°, the band angle is higher than observed in experiments (15); this inconsistency requires further investigation. The other variable in the simulations is the magnitude of viscous anisotropy. In all four simulations, α increases from zero at the center of the cylinder to $\alpha_{\max} = 2$ at $r \approx 1$ mm and then remains constant at larger radii. In two of the simulations, β mimics the behavior of α. In the other two simulations, β is zero at all radii. In the decompaction region (i.e., at small radii), profiles with Θ = 45° exhibit higher melt fractions than

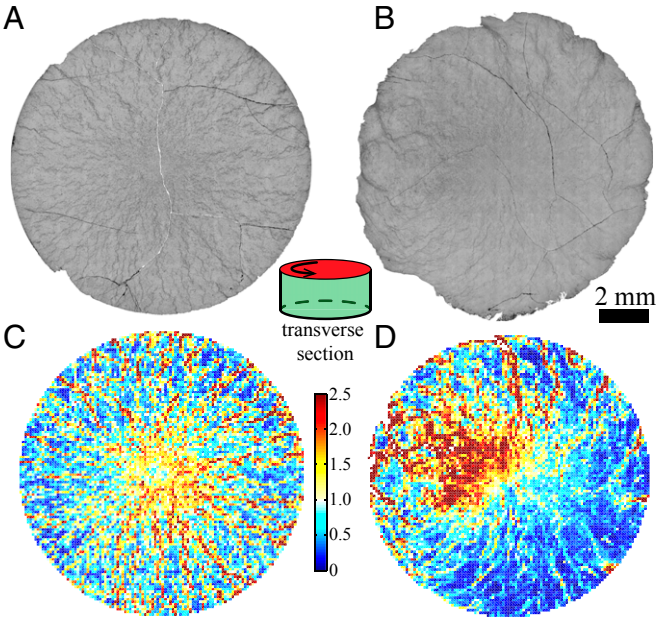

Fig. 3. Optical micrographs and processed images demonstrating base-state melt segregation. (*A* and B) Optical micrographs of transverse sections from samples sheared to $\gamma(R) =$ 5.0 (PI0817) and 14.3 (PI0891), respectively. Olivine is light gray and melt is dark gray. The sketch located between *A* and *B* is a deformed cylindrical sample with its transverse section marked in red. (*C* and *D*) Melt distribution maps generated from *A* and *B*, respectively. The grid size is 100 × 100 μm^2. Color bar indicates melt fraction normalized to the average melt fraction in the image. Due to its high strain, sample PI0891 sheared off axis so that the torsional axis is to the northwest of the center of the image.

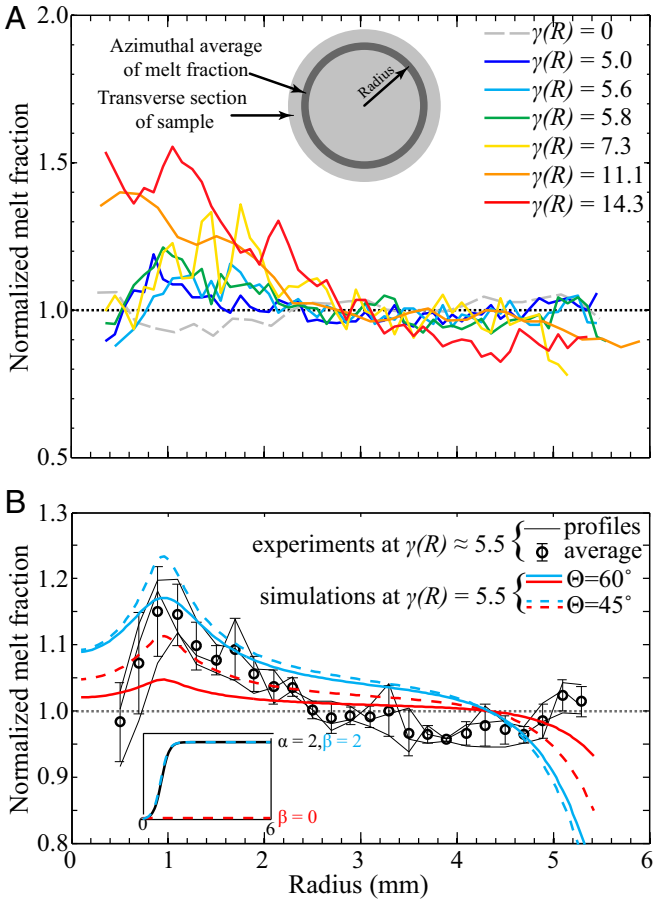

Fig. 4. Azimuthally averaged, normalized melt fraction vs. radius. (*A*) Plot of azimuthally averaged, normalized melt fraction vs. radius for starting material and six deformed samples. *Inset* shows the outer-radius strain of each sample. Melt fraction is normalized by the average value of the transverse section of each sample. The black dotted line corresponds to a normalized melt fraction of 1.0. The sketch shows how an azimuthal average of melt fraction is obtained for a given radius. (*B*) Reproducibility test for three samples sheared to $\gamma(R) = 5.5 \pm 0.5$ and its comparison with the results from numerical simulations. Simulations were conducted with an initial compaction length of $\delta_c = 0.1R$, a bulk-to-shear viscosity ratio of $r_\xi = 10$, anisotropy angles of $\Theta = 60°$ and 45°, and anisotropy magnitudes $\alpha(r)$ and $\beta(r)$ shown in *Inset*. Blue lines are for the case with $\alpha_{max} = 2$ and $\beta_{max} = 2$, and red lines are for the case with $\alpha_{max} = 2$ and $\beta = 0$. There was no initial porosity perturbation and hence no band formation. Further details are provided in *SI Appendices 1* and *2*.

those with $\Theta = 60°$, whereas profiles with $\alpha_{max} = \beta_{max} = 2$ exhibit higher melt fractions than those with $\alpha_{max} = 2$ and $\beta = 0$. The profile with $\Theta = 60°$ and $\alpha_{max} = \beta_{max} = 2$ is the most consistent with the experimental results. However, some clear differences exist between the simulated and the experimental profiles. First, for $2.6 < r < 4.4$ mm the simulated profiles lie above the experimentally measured profile. Second, the abrupt decrease in the simulated profiles at $r > 4.4$ mm was not observed experimentally. Despite these quantitative discrepancies, all simulated porosity profiles are in good qualitative agreement with those from experiments, in terms of both the amplitude and the radial position of the porosity maximum.

Conclusions

In this paper we presented experimental observations of the radial distribution of melt in partially molten rocks deformed in torsion to large strain. For this deformation geometry, the theory of melt segregation with anisotropic viscosity predicts a radial distribution of melt fraction. The inclusion of viscous anisotropy in the theory is a necessary and sufficient condition for the development of radially inward, base-state melt segregation. Our experiments test this prediction, and the results reported here are in general agreement with theory, validating the viscous-anisotropy hypothesis. This experimental validation of MPO-induced viscous anisotropy represents a significant advance in our understanding of the relationship between microstructure and continuum mechanics of partially molten rocks, and it also exposes details of the linkage between deformation, MPO, and viscosity that are not captured by the present model. Although questions remain concerning the influence of MPO-induced viscous anisotropy on large-scale mantle dynamics, this study emphasizes its importance to melt segregation and rheological behavior of partially molten rocks in laboratory experiments and mantle flow.

Materials and Methods

Samples were fabricated from mixtures of fine-grained powders of olivine from San Carlos, AZ, plus 10 vol% alkali basalt from Hawaii (20). Olivine powders were obtained by grinding San Carlos olivine crystals in a fluid-energy mill to produce a particle size of 2 μm. Before mechanically mixing with alkali basalt powders with a particle size of ∼10 μm, the olivine powders were dried at 1,373 K for 12 h at an oxygen partial pressure near the Ni-NiO buffer to remove water and carbon-based impurities introduced during the grinding process. Mixtures were uniaxially cold-pressed at 100 MPa into nickel capsules and then hydrostatically hot-pressed at 1,473 K and 300 MPa for 3.5 h in a gas-medium apparatus (21). After hot-pressing, samples were cut into thin cylinders with a diameter of $2R \approx 12$ mm and a thickness of 3–5 mm. The cut sample was then placed into a nickel capsule with spacers cored from a coarse-grained natural dunite as end caps, thus providing nonreactive, impermeable boundaries during deformation (22). The sample, Al_2O_3 spacers and pistons, and ZrO_2 pistons were enclosed in an iron jacket for deformation.

Torsion experiments were conducted at a shear strain rate of $10^{-3.5} s^{-1}$, a temperature of 1,473 K, and a confining pressure of 300 MPa in a gas-medium apparatus fitted with a torsion actuator (21). After achieving the target strain, each sample was cooled rapidly (∼2 K/s) to 1,300 K under the torque imposed at the end of the deformation experiment to preserve the deformation-produced microstructure and then cooled to room temperature with no torque applied. After deformation, with the iron jacket and the nickel capsule dissolved in acid, the deformed sample was cut in half perpendicular to the torsional axis, leaving two transverse sections for examination. Each transverse section was polished on a series of diamond lapping films down to 0.5 μm, followed by a final step using colloidal silica. The section was then examined by reflected-light optical microscopy after chemically etching with diluted HF to highlight melt pockets.

To map the whole transverse section with an area of ∼113 mm^2, a mosaic image consisting of 2,209 high-resolution (0.3 μm per pixel) optical micrographs was used. A binary image with melt appearing white was created from this mosaic image, using a combined image segmentation method, which includes edge detection (23–25) and a threshold of grayscale. Then a profile of melt fraction was calculated from the area fraction of the white pixels (22).

ACKNOWLEDGMENTS. The authors thank Mark Zimmerman and Matěj Peč for help with experiments and analyses; Yan Liang and Clint Conrad for providing the alkali basalt; and Dan McKenzie, Dave Stevenson, and Wen-lu Zhu for their valuable comments. Numerical models were run on ARCHER, the United Kingdom national supercomputer. This study was supported by National Science Foundation Grant EAR-1214876. The research leading to these results has received funding from the European Research Council (ERC) under the European Union's Seventh Framework Programme (FP7/2007C2013)/ERC Grant 279925. R.F.K. is grateful to the Leverhulme Trust for support.

1. Stevenson D (1989) Spontaneous small-scale melt segregation in partial melts undergoing deformation. *Geophys Res Lett* 16:1067–1070.
2. Holtzman B, Groebner N, Zimmerman M, Ginsberg S, Kohlstedt D (2003) Stress-driven melt segregation in partially molten rocks. *Geochem Geophys Geosyst* 4(5): 8607.
3. King D, Zimmerman M, Kohlstedt D (2010) Stress-driven melt segregation in partially molten olivine-rich rocks deformed in torsion. *J Petrol* 51:21–42.
4. Kohlstedt D, Holtzman B (2009) Shearing melt out of the earth: An experimentalist's perspective on the influence of deformation on melt extraction. *Annu Rev Earth Planet Sci* 37:561–593.

5. Kendall JM (1994) Teleseismic arrivals at a mid-ocean ridge: Effects of mantle melt and anisotropy. *Geophys Res Lett* 21:301–304.
6. Kawakatsu H, et al. (2009) Seismic evidence for sharp lithosphere-asthenosphere boundaries of oceanic plates. *Science* 324(5926):499–502.
7. Spiegelman M (2003) Linear analysis of melt band formation by simple shear. *Geochem Geophys Geosyst* 4(9).
8. Katz RF, Spiegelman M, Holtzman B (2006) The dynamics of melt and shear localization in partially molten aggregates. *Nature* 442(7103):676–679.
9. McKenzie D (1984) The generation and compaction of partially molten rock. *J Petrol* 25(3):713–765.
10. Takei Y, Holtzman B (2009) Viscous constitutive relations of solid-liquid composites in terms of grain boundary contiguity: 1. Grain boundary diffusion control model. *J Geophys Res* 114(B6):B06205.
11. Takei Y, Holtzman B (2009) Viscous constitutive relations of solid-liquid composites in terms of grain boundary contiguity: 2. Compositional model for small melt fractions. *J Geophys Res* 114(B6):B06206.
12. Butler S (2012) Numerical models of shear-induced melt band formation with anisotropic matrix viscosity. *Phys Earth Planet Inter* 200:28–36.
13. Takei Y, Katz RF (2013) Consequences of viscous anisotropy in a deforming, two-phase aggregate. Part 1. Governing equations and linearized analysis. *J Fluid Mech* 734:424–455.
14. Takei Y, Holtzman B (2009) Viscous constitutive relations of solid-liquid composites in terms of grain boundary contiguity: 3. Causes and consequences of viscous anisotropy. *J Geophys Res* 114(B6):B06207.
15. Katz RF, Takei Y (2013) Consequences of viscous anisotropy in a deforming, two-phase aggregate. Part 2. Numerical solutions of the full equations. *J Fluid Mech* 734: 456–485.
16. Cooper RF, Kohlstedt DL (1986) Rheology and structure of olivine-basalt partial melts. *J Geophys Res* 91:9315–9323.
17. Zimmerman ME, Zhang S, Kohlstedt DL, Karato SI (1999) Melt distribution in mantle rocks deformed in shear. *Geophys Res Lett* 26:1505–1508.
18. Holtzman B, Kohlstedt D (2007) Stress-driven melt segregation and strain partitioning in partially molten rocks: Effects of stress and strain. *J Petrol* 48(12):2379–2406.
19. Takei Y (2010) Stress-induced anisotropy of partially molten rock analogue deformed under quasi-static loading test. *J Geophys Res Solid Earth* 115(B3):1978–2012.
20. Morgan Z, Liang Y (2003) An experimental and numerical study of the kinetics of harzburgite reactive dissolution with applications to dunite dike formation. *Earth Planet Sci Lett* 214:59–74.
21. Paterson M, Olgaard D (2000) Rock deformation tests to large shear strains in torsion. *J Struct Geol* 22:1341–1358.
22. Qi C, Zhao YH, Kohlstedt DL (2013) An experimental study of pressure shadows in partially molten rocks. *Earth Planet Sci Lett* 382:77–84.
23. Canny J (1986) A computational approach to edge detection. *IEEE Trans Pattern Anal Mach Intell* 8(6):679–698.
24. Lim J (1990) *Two-Dimensional Signal and Image Processing* (Prentice Hall, Englewood Cliffs, NJ).
25. Parker J (2010) *Algorithms for Image Processing and Computer Vision* (Wiley, Indianapolis).